A Generalized Deep Learning-Based Method for Rapid Co-Seismic Landslide Mapping

Jing Yang, Mingtao Ding, *Member, IEEE*, Wubiao Huang, Zhenhong Li, *Senior Member, IEEE*,
Zhengyang Zhang, Jing Wu, and Jianbing Peng

***Abstract*—The rapid mapping of co-seismic landslides is essential for emergency management and loss assessment. Deep learning algorithms generally follow a supervised learning workflow, where the trained model is used to predict landslides in surrounding areas, achieving landslide mapping with high accuracy. For a new study area landslide extraction task, the performance of the model trained on a specific dataset will be greatly reduced due to the varying data distribution of co-seismic landslides. Considering the urgent need for large-scale co-seismic landslide mapping, we developed a generalized deep learning-based landslide identification method. First, a new model—ResU-SENet is developed to generate semantic segmentation maps of landslides. The proposed model adaptively emphasizes the channel-wise weights of the input data. Three multidomain models are then designed by combining annotated landslide samples from two different domains to improve the model generalization ability. Finally, the trained models are applied directly to completely unknown domains to test model generalizability. Experiments in Iburi and Jiuzhaigou showed that the proposed model yielded the recall values of 5.93% and 7.51% higher than ResU-Net. The adoption of multidomain models effectively reduced the number of new training samples required by 50% and maintained a similar identification performance as if trained entirely with new samples. Applying the models trained by Jiuzhaigou and Iburi samples directly to Palu, the F1-score under the ResU-SENet model reached 0.6875. Moreover, the connections between model generalization and data distribution was demonstrated. This work could provide a fast response for future large-scale co-seismic landslide mapping.**

***Index Terms*—Change detection, co-seismic landslide inventory mapping, generalization, landslide identification, medium-resolution imagery, multidomain trained model, semantic segmentation.**

I. Introduction

As a common and frequent secondary geological hazard of earthquakes, co-seismic landslides usually cause surface rupture, which not only makes emergency rescue difficult but also causes serious economic losses [1], [2]. For instance, the M_w 7.8 earthquake that struck Turkey on February 6, 2023, resulted in over 40 000 fatalities due to landslide disasters. Due to the characteristics of large-scale, powerful destructiveness and wide distribution of co-seismic landslide, the landslide hazard analysis is inseparable from co-seismic landslide inventory maps [3]. Reliable co-seismic landslide inventories further provide the theoretical underpinning for preventing and controlling geological disasters, as well as for facility location and facility layout [4].

Scientists have taken note of the challenges that co-seismic landslide mapping continues to face: accuracy and timeliness. The traditional method of landslide detection, which relies on field surveys, is frequently impeded by harsh environments and inaccessible high mountainous areas, making it inefficient and resulting in poor accuracy of landslide mapping. Afterward, various landslide mappings have been developed using remote sensing images. Landslide inventory maps were initially created through visual interpretation. This method was criticized as being labor- and time-intensive, especially when mapping large areas [5]. Later, the advent of semiautomated landslide detection techniques compensates for the weaknesses of visual interpretation and can be categorized as either pixel-based or object-based methods. Change detection technique is the commonly used pixel-based landslide detection method [5], [6], [7]. Landslides are regarded as land cover changes through pre- and post-images. Ancillary datasets, such as digital elevation models (DEMs) and the Normalized Difference Vegetation Index (NDVI), are applied to improve the accuracy of landslide identification [8], [9], [10]. However, pixel-based landslide mapping relies solely on the spectral characteristics of individual pixels and is sensitive to noise [11]. Object-oriented analysis exploits the content information of local pixel neighborhoods, but it is highly dependent

Received 16 April 2024; revised 15 July 2024; accepted 3 September 2024. Date of publication 11 September 2024; date of current version 30 September 2024. This work was supported in part by the National Natural Science Foundation of China under Grant 41941019 and Grant 42374027, in part by the National Key Research and Development Program of China under Grant 2021YFC3000400, in part by the Opening Fund of Key Laboratory of Smart Earth under Grant KF2023YB04-01, in part by the Application and Demonstration of Comprehensive Governance and Scale Industrialization in the Sichuan-Tibet Region under the High-resolution Satellite Project under Grant 87-Y50G28-9001-22/23, in part by Key R&D Program Projects in Zhejiang Province under Grant 2023C03177, and in part by the Fundamental Research Funds for the Central Universities under Grant 300102262203. *(Jing Yang and Mingtao Ding are co-first authors.) (Corresponding author: Zhenhong Li.)*

Jing Yang is with the College of Geological Engineering and Geomatics, Chang'an University, Xi'an 710054, China, and also with the Qinghai Institute of Technology, Xining 810000, China (e-mail: 2020126052@chd.edu.cn).

Mingtao Ding, Zhenhong Li, and Jianbing Peng are with the College of Geological Engineering and Geomatics, Chang'an University, Xi'an 710054, China, also with the Key Laboratory of Loess, Xi'an 710054, China, and also with the Key Laboratory of Western China's Mineral Resource and Geological Engineering, Ministry of Education, Xi'an 710054, China (e-mail: mingtaoding@chd.edu.cn; zhenhong.li@chd.edu.cn; dicexy_1@chd.edu.cn).

Wubiao Huang is with the School of Geodesy and Geomatics, Wuhan University, Wuhan 430072, China (e-mail: huangwubiao@whu.edu.cn).

Zhengyang Zhang is with the College of Geological Engineering and Geomatics, Chang'an University, Xi'an 710054, China (e-mail: 2020900247@chd.edu.cn).

Jing Wu is with the Qinghai Institute of Geo-Environment Monitoring, Xining 810008, China (e-mail: endless5wj@163.com).

Digital Object Identifier 10.1109/JSTARS.2024.3457766

on the segmentation scale and optimal parameter values and requires high spatial resolution images [12].

Deep learning (DL) has been extensively employed in image classification, including handwriting recognition, face recognition, and medical diagnosis. The similarity between natural images and remote sensing images makes the remote sensing image processing based on DL algorithms possible. In 2014, Long et al. [13] proposed fully convolutional networks (FCNs), which enabled the end-to-end, pixel-level image classification [14]. Various deformed semantic segmentation models, such as U-Net [15], SegNet [16], and the DeepLab series [17], have been employed for landslide identification based on FCN. Liu et al. [18] ultilized the Google Earth Engine (GEE) platform and U-Net for co-seismic landslide recognition. Yu et al. [19] proposed a two-branch Matrix SegNet for landslide semantic segmentation using change detection with images of different spatial resolutions. Lu et al. [20] developed a dual-encoder U-Net for landslide mapping and achieved a maximum F1-score of 79.24%, outperforming SegNet, U-Net, and Attention U-Net. Gao et al. [14] proposed the FC-DenseNet, which repeatedly uses extracted features in a dense structure and incorporates landslide influencing factors. The results demonstrate that FC-DenseNet has great potential for landslide detection and mapping [14]. In this work, ResU-Net [21] has been used as the benchmark network. Considering that different geomorphic units have varying contributions to the occurrence of landslides, and the abundance of channel redundancy information in skip connections between the encoder and decoder, a new model namely ResU-SENet was proposed.

The superior performance of DL in landslide mapping is driven by a large number of labeled landslide training samples. In reality, accessing the annotated landslide samples of all co-seismic events is a resource-intensive and challenging process. When the probability distributions of training data and testing data are different due to domain gaps, such as environmental conditions and imaging conditions, the performance of DL models often deteriorates. Therefore, it is urgent to investigate the transferability of models. Domain adaptation (DA) as a specific form of transfer learning, aims to align the data distribution between different domains, whereby reducing the domain discrepancy and enabling the model to perform well in a completely new domain [22]. When the target domain has no annotated label, the task is called unsupervised DA (UDA). Several scholars have introduced UDA to solve the problem of cross-domain landslide mapping. Xu et al. [23] applied an adversarial learning-based DA network which is called ANANet to perform different co-seismic landslide identification task and an output space adaptation strategy is adopted. It mainly focuses on single-source to single-target DA. Considering landslides in different domains have different triggering factors, imaging conditions, and topography, Zhang et al. [24] proposed a prototype-guided domain-aware progressive representation learning framework for landslide mapping from multiple heterogeneous domains. Qin et al. [25] used distant domain transfer learning for landslide mapping, which requires labeled landslide data and unlabeled data from completely different domains. Other studies have trained landslide identification models by constructing multidomain datasets that contain training samples from different domains to enhance model generalization capability [26], [27]. Meena et al. [26] selected landslide samples from 10 different geographical environment domains and constructed a landslide detection dataset, and the generalization of the dataset was tested on newly occurring landslide events. Prakash et al. [27] proposed a generalized CNN, wherein landslide models were trained on multiple geographic domains and achieved a superior performance to single domains. However, these previous studies simply combined all the landslide samples without considering the relationship between data distribution and model efficiency. Moreover, the existing landslide datasets are mainly true-color images constructed by RGB bands, topographic factors and spectral information were not fully utilized.

In this work, we achieved the model generalization ability through multidomain training and revealed the connections between the model generalization and data distribution. This not only substantially reduces the number required to annotate new labels but also provides a guideline for model selection based on data distribution. Meanwhile, four co-seismic landslide datasets have been constructed, making full use of spectral and topographic information.

The term "domain" represents landslide satellite datasets from different geographical environments, illumination conditions, and imaging conditions. There are three domains in this work: 1) the Iburi domain **(Ib)**, 2) the Jiuzhaigou domain **(J)**, and 3) the Palu domain **(P)**. Depending on the experimental setup, the domains are further divided into "known" domains and "unknown" domains. The "known" domains represent the regions used to train the models (i.e., Iburi and Jiuzhaigou). The "unknown" domains are not used for training models but rather are used directly to test model generalizability (i.e., Palu). The term "sample" means landslide or nonlandslide patches that were selected for model training, validation, and testing. Each sample represents a specific landslide event, characterized by landslide triggers, geographical location, and imaging conditions. Sample is the basic unit of model training and its quality significantly determines the model performance. Multidomain models represent a combination of landslide training samples from two known areas. When constructing a multidomain model, according to the experimental setup, the two known domains are referred to as the local domain and the foreign domain, respectively.

The main contributions of this study can be summarized as follows.

1) A new segmentation network called ResU-SENet has been proposed for landslide inventory mapping. The model adaptively emphasizes the contribution weights of each input channel to the occurrence of landslides.
2) Reference landslide inventories were created for co-seismic landslide domains and the landslide label generation process was automated, based on the ArcGIS platform. Multichannel landslide datasets were produced for landslide mapping.
3) Landslide identification multidomain models were proposed by combining annotated landslide labels from different domains. Samples from Jiuzhaigou and Iburi were selected to train the benchmark model and multidomain

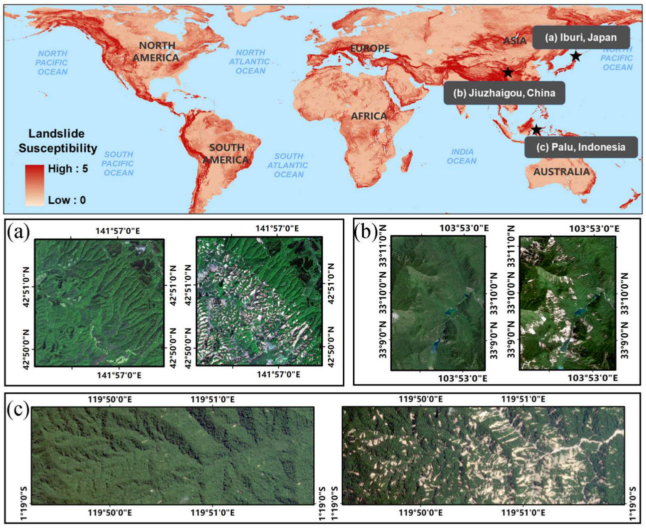

Fig. 1. Geographical location of each study area and Sentinel-2 images corresponding to pre- and postearthquake images. (a) Iburi. (b) Jiuzhaigou. (c) Palu.

TABLE I
KEY INFORMATION OF CO-SEISMIC LANDSLIDES DATASETS

Study area		Iburi (Ib)	Jiuzhaigou (J)	Palu (P)
Epicenter		42.72°N, 142.0°E	33.20°N, 103.82°E	0.22°S, 119.85°E
Study area		683.86 km^2	919.804 km^2	2488.39 km^2
Acquisition date	pre	2017-06-17	2017-07-29	2018-07-14
	post	2019-05-23	2017-09-07	2019-09-17
Sample	train	700	700	--
	test	300	300	109
Number of landslides		7197	2021	3436

model and were directly used to test generalization ability in Palu domains.

4) The impact of data distribution on model generalization performance is discussed.

It is noteworthy that, when the model proposed in this article are directly applied to the 2022 Luding co-seismic landslide, good results are also obtained. Precision, recall, F1-score, Matthews correlation coefficient (MCC), and Intersection over Union (IoU) were utilized to compare the robustness of these models.

II. STUDY AREA AND DATA

In this work, we selected three co-seismic landslide regions as study areas. To take advantage of the free Sentinel-2 imagery, we deliberately selected co-seismic events after mid-2015. This ensured that the models generated from this work could be applied to landslide mapping in new areas based on freely available imagery. Each study area's geographic location is displayed in Fig. 1, together with pre- and postearthquake Sentinel-2 images with RGB synthesis. Table I summarizes the key information for each earthquake.

A. Iburi Earthquake

On September 6, 2018, an Mw 6.6 earthquake struck the Tobu area of Iburi, Hokkaido, Japan. The shock induced at least 6000 landslides, most of which were shallow landslides [28]. In this work, the study area extends to an area of 683.86 km^2, with elevations ranging between 0 and 625 m. Two cloud-free Sentinel-2 images were acquired on June 17, 2017 and May 23, 2019, respectively. The existing Iburi landslide inventory [29] was then modified, creating a closer match between landslide boundaries and Sentinel-2 images. A total of 7197 landslides were mapped with areas ranging from 24 m^2 to 0.205 km^2.

B. Jiuzhaigou Earthquake

An M_w 7.0 earthquake with a focal depth of 20 km occurred in the north of Sichuan Province, China on August 8, 2017. More than 1700 aftershocks occurred over the next 36 hours, causing landslides that removed vegetation and exposed many hillsides [30], [31]. Several landslide inventories triggered by the Jiuzhaigou earthquake have been mapped using high-resolution imagery [30], [32]. Taking these inventories as a reference, we selected 919.804 km^2 as the study area and created a new landslide inventory by way of the pre- and postevent images from July 29, 2017 and September 7, 2017, by which to train the DL models. From the optical images, we found that landslides in Jiuzhaigou were characterized by varying sizes, complex shapes, and confusion with surrounding features. From the inventory map, we found that the spatial distribution of landslides is mostly located in the northwest and southeast of the epicenter. Since some landslides were covered by clouds in the pre-event image, 2021 landslides were ultimately identified, with areas ranging from 22 m^2 to 0.385 km^2.

C. Palu Earthquake

On September 28, 2018, a mega-earthquake (M_w 7.5) struck in the Palu region of central Sulawesi, Indonesia [33]. Massive co-seismic landslides were caused particularly in nearby mountainous regions [34]. In this work, we selected a surface area of 2488.39 km^2 near the Palu Basin as our study area, with elevations ranging from sea level to approximately 2485 m. To establish the landslide inventory in Palu, bitemporal images were collected on July 14, 2018 and September 17, 2019, respectively. Then, they were utilized to identify the main landslide concentration areas. Finally, 3436 co-seismic landslides were interpreted, with areas ranging from 40 m^2 to 0.312 km^2, which were used to test the model's generalization ability.

D. Data Preparation

1) Sentineal-2 Data and Topographic Factors: We collected optical data from the Sentinel-2 satellite and DEMs from the Shuttle Radar Topography Mission for landslide identification. Based on the principle of minimal cloud cover, which corresponds to bitemporal for each study area, a total of eight Level-1C images were chosen. NDVI as a crucial index that reflects the vegetation growth status is susceptible to vegetation loss which may be caused by landslides. Therefore, NDVI images corresponding to pre- and postevent were added as extra channels to overcome the drawbacks of responding to landslides detected with RGB spectral data only. It is defined as follows:

$$\mathrm{NDVI} = \frac{\mathrm{NIR} - \mathrm{RED}}{\mathrm{NIR} + \mathrm{RED}} \tag{1}$$

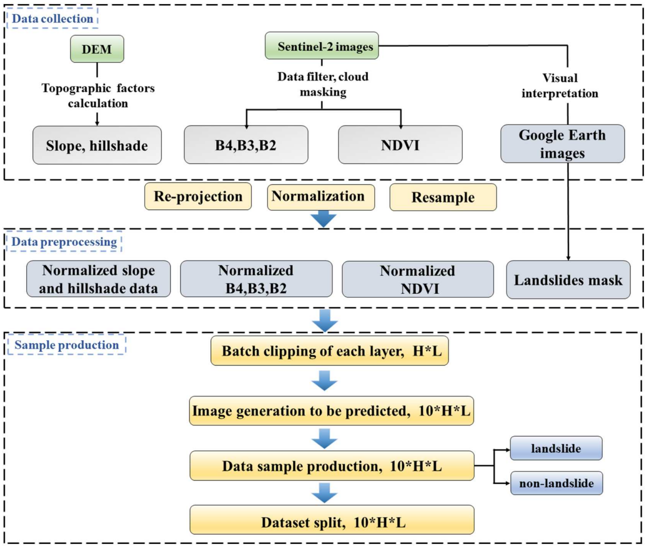

Fig. 2. Sample production process.

where NIR and RED are the reflectance of the near-infrared and red bands.

The steepness of the slope is a crucial topographic factor that directly affects the movement of landslides [35]. Hillshade is another topographic factor that has been extensively applied in landslide mapping [36], [37]. Hillshade maps and slope were derived from DEM, and these topographic factors were added as ancillary data to enhance the model performance.

The topography and imagery data utilized in this work were provided via the GEE platform, which is a cloud-based platform that allows easy access to remote sensing imagery and the processing of large geospatial datasets using online computing resources [38].

Finally, there are ten input bands of the same resolution (10 m) in each study area: slope, hillshade, pre-event red band, postevent red band, pre-event green band, postevent green band, pre-event blue band, postevent blue band, pre-event NDVI, and postevent NDVI. On the other hand, the landslide inventories in each study area were interpreted using Sentinel-2 images and the ArcGIS platform. Detailed information is presented in Table I.

2) Generation of Dataset: According to the workflow of sample production in Fig. 2, we first added a geographic coordinate system to the collected data and resampled the data to 10-m resolution by way of bilinear interpolation. We then normalized the images using a max–min normalization approach to facilitate the proposed network training. As for the sample production, we exploited the toolbox integrated into the ArcGIS platform, which can rapidly generate DL samples [39]. This toolbox integrates all landslide sample generation operations into the ArcGIS platform, rather than requiring users to work across platform. This not only simplifies the complex sample generation process but is particularly useful for the multiple regions considered in this aticle. Predominantly, four tools were used: "Batch Clipping of Each Factor Layer," "Image Generation to be Predicted," "Data Sample Production," and "Dataset Split." Table II details the functions of each tool.

TABLE II
MAIN TOOLS AND FUNCTIONS FOR SAMPLE PRODUCTION

Tools	Function
Batch Clipping of Each Factor Layer	Batch clip the input ten bands to the same number of rows and columns
Image Generation to be Predicted	Stack the ten clipped bands to form multi-channel raster data
Data Sample Production	Generate model training samples based on vector border data
Dataset Split	Split samples into training set and test set in a certain ratio

The training of numerous trainable parameters in DL is driven by a large number of labeled samples [40]. Data augmentation strategies can broaden the training dataset variety, which also helps in regularizing the trained model to improve generalization [41], [42]. We expanded the Iburi and Jiuzhaigou training datasets, exploiting horizontal flip, diagonal mirroring, and vertical flip respectively. The number of samples ultimately obtained was 1656 for Iburi and 1056 for Jiuzhaigou, including positive and negative samples. Meanwhile, keeping the balance of positive and negative samples reduces overfitting and improves the accuracy of landslide identification. The Palu samples were used only to test the model's generalization ability, and thus there were 109 samples for Palu and no data augmentation.

III. METHODOLOGY

For the study of model generalization, first, a novel semantic segmentation network named ResU-SENet has been proposed to achieve precise landslide extraction. Confronted with multiple co-seismic scenes mentioned in the article, we choose to train several multidomain models by mixing samples from two distinct source domains to validate the model generalization on the target domain based on ResU-SENet.

A. Proposed ResU-SENet Network Architecture

With the purpose of extracting landslide from multichannel remote sensing dataset, an efficient DL model is indispensable. Existing landslide semantic segmentation models are mainly encoder–decoder structures. However, as the encoder progressively up-samples and extracts features, the details of small targets are seriously lost, and there is a lack of local context information. To address this problem, skip connections have been proposed to preserve the data details and semantic information of raw data. Given the complex spectral characteristics, spatial distributions, and scales of co-seismic landslides in different domains, and there is a lot of channel redundancy information in skip connection, it is important to adaptively emphasize the contribution of channels to the occurrence of landslide, for the effective propagation of low-level features.

Therefore, a new landslide identification network called ResU-SENet was proposed (see Fig. 3). Three components make up the network: an encoder, a decoder, and a bridge connecting the encoder and decoder. The encoder and decoder parts are to extract different features and precisely segmentation using ResU-Net [21]. The channel-wise attention mechanism, SE module [43] was embedded into the skip connection to adaptively obtain the importance of each low-level feature channel and pass it to the high-level features. Finally, the landslide

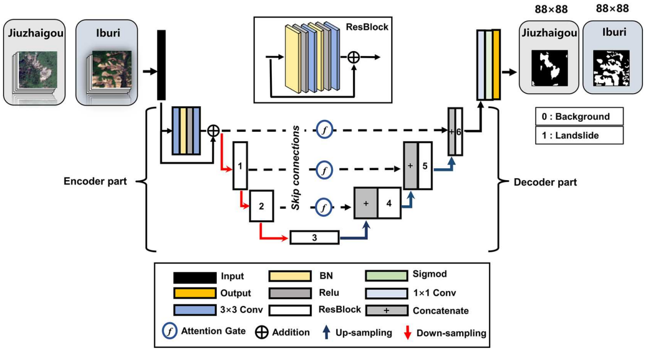

Fig. 3. Architecture of proposed ResU-SENet.

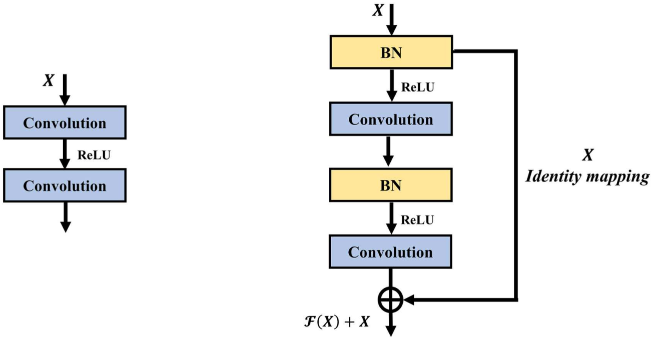

Fig. 4. Comparisons of plain neural unit (left) and residual unit (right) [21].

TABLE III
DETAILED INFORMATION ON RESU-SENET STRUCTURE

Name	Kernel size	Stride	Output size
Input	--	--	88×88×10
Conv	3×3/64	1	88×88×64
Conv	3×3/64	1	
ResBlock_1	3×3/64	2	44×44×64
	3×3/64	1	
ResBlock_2	3×3/128	2	22×22×128
	3×3/128	1	
ResBlock_3	3×3/256	2	11×11×256
	3×3/256	1	
Attention _1	--	--	22×22×256
Concat_1	--	--	22×22×768
ResBlock_4	3×3/256	1	22×22×256
	3×3/256	1	
Attention _2	--	--	44×44×256
Concat_2	--	--	44×44×768
ResBlock_5	3×3/256	1	44×44×256
	3×3/256	1	
Attention _3	--	--	88×88×128
Concat_3	--	--	88×88×384
ResBlock_6	3×3/128	1	88×88×128
	3×3/128	1	
Conv	1×1	1	88×88

segmentation map was obtained by way of the classification layer.

The encoder part, also known as the feature extractor, consists of three residual units, as proposed by He et al. [44]. Compared with a plain neural unit, the outstanding characteristic of a residual block is shortcutting and identity mapping, effectively alleviating gradient vanishing and improving the depth of the trained network [44]. Fig. 4 shows the structural differences between the plain neural unit and the residual unit. The residual unit predominantly consists mainly of convolutional layers, activation layers, and max-pooling layers. The convolutional layers extract features from the input through convolutional operations. As the number of iterations increases, the convolutional layers extract higher-level features. The nonlinear activation layer improves the expressiveness of the model by adding nonlinear factors to linear convolutional layers through nonlinear functions. In this work, rectified linear unit function was chosen. The pooling layer effectively reduces the size of the parameter matrix and accelerates the model training. After each down-sampling step, the input feature size is reduced by half and the channel is doubled. Correspondingly, the decoder part is also composed of three residual units. The decoder concatenated the features from the encoder (dashed arrows in Fig. 3) and transferred the merged array to subsequent residual units for improved localization while restoring the image size. Through continuous iteration and backward propagation, the model parameters are trained and adaptively tuned. Finally, a 1×1 convolution layer and sigmoid activation layer are used to generate landslide segmentation maps.

Skip connection is frequently utilized in U-shape networks to connect the high-level and low-level features. However, there is often much redundancy information in low-level features. As a typical implementation of the channel attention mechanism, the SE module focuses on the weight of each channel layer. It consists of squeeze (sq), excitation (ex), and scale. For the input features, the squeeze part is first operated in the spatial dimension through channel global average pooling. The weights are then learned through two fully-connected layers and a sigmoid function in the excitation part, with weight values constrained between 0 and 1. Finally, the scale part utilizes the learned weights to reweigh the importance of each channel.

Three SE modules are strategically embedded within the skip connection architecture. The first module is designed to reweight the landslide edge and color characterizes, enhancing the low-level feature representations. The second was designed after the output of Rseblock1 to highlight texture details specific to landslide. The final SE module was positioned after the output of Resblock2, and aimed to reweight the abstract high-level semantic features. Through continuous iteration and learning of the model, the greater the channel's contribution to the landslide occurrence, the greater its channel weight, and consequently the landslide identification accuracy will increase.

The proposed ResU-SENet model allows the network to focus on valuable features and suppress irrelevant features, to adaptively obtain the importance of each feature channel through learning and improve network performance. Table III lists detailed information on the proposed ResU-SENet model.

Landslide pixels always account for a small proportion of the sample, resulting in the predictions being strongly biased toward the background [45]. Thus, the dice loss function [45]

TABLE IV
CONFUSION MATRIX

Classification	Prediction results	Actual results
TP	landslide	landslide
FP	landslide	non-landslide
TN	non-landslide	non-landslide
FN	non-landslide	landslide

TABLE V
TRAINED MODEL IN THIS STUDY

Trained Model	Training domain composition
Ib700	100% Iburi(benchmark)
J700	100% Jiuzhaigou(benchmark)
Ib200J500	28%Iburi 72%Jiuzhaigou
Ib350J350	50%Iburi 50%Jiuzhaigou
Ib500J200	72%Iburi 28%Jiuzhaigou

TABLE VI
LANDSLIDE IDENTIFICATION RESULTS BASED ON RESU-NET AND RESU-SENET

Domain	Detector	Model	Precision	F1-score	Recall	MCC	IoU
Iburi	Ib700	ResU−Net	0.8936	0.8246	0.7775	0.7908	0.7073
		ResU−SENet	**0.8766**	**0.853**	**0.8368**	**0.8175**	**0.7460**
Jiuzhaigou	J700	ResU−Net	0.8051	0.7532	0.7190	0.7097	0.6085
		ResU−SENet	**0.7880**	**0.7876**	**0.7941**	**0.7449**	**0.6545**

The bold values represents better results compared to others.

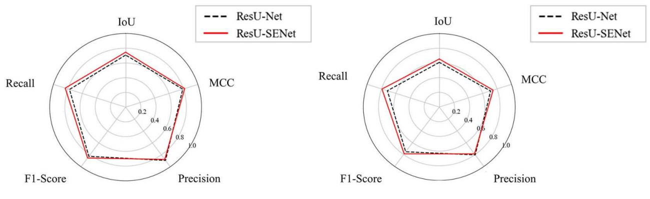

(a) (b)

Fig. 5. Comparison of robustness of ResU-Net and ResU-SENet in different domains. (a) Iburi. (b) Jiuzhaigou.

was adopted in place of the more commonly used binary cross-entropy

$$\text{Dice loss} = 1 - \frac{2\Sigma_i^h \Sigma_j^w p_{i,j} g_{i,j} + \epsilon}{\Sigma_i^h \Sigma_j^w p_{i,j} + g_{i,j} + \epsilon} \tag{2}$$

where h and w represent the height and width, i and j represent the row and column number of pixels, $p_{i,j}$ is the predicted map and $g_{i,j}$ is the ground truth label; and ϵ is a tiny constant to avoid the denominator being zero. From Formula (2), we can see that nonlandslide areas with values equal to 0 are neglected, attenuating the imbalance between positive and negative pixels.

B. Validation Indexes

When evaluating the model performance in binary classification, predicted labels are often compared with ground truth labels [46], resulting in four kinds of classified pixels: true positive (TP), false positive (FP), false negative (FN), and true negative (TN). Table IV shows the composition of confusion matrix.

Based on these values, five commonly used evaluation metrics were adopted—precision, recall, F1-score, IoU, and MCC and are defined as

$$\text{Precision} = \frac{\text{TP}}{\text{TP} + \text{FP}} \tag{3}$$

$$\text{Recall} = \frac{\text{TP}}{\text{TP} + \text{FN}} \tag{4}$$

$$\text{IoU} = \frac{\text{TP}}{\text{TP} + \text{FP} + \text{FN}} \tag{5}$$

$$\text{F1} - \text{score} = 2 \times \frac{\text{Precision} \times \text{Recall}}{\text{Precision} + \text{Recall}} \tag{6}$$

$$\text{MCC} = \frac{\text{TP} \times \text{TN} - \text{FP} \times \text{FN}}{\sqrt{(\text{TP} \times \text{FP})\,(\text{TP} \times \text{FN})\,(\text{TN} \times \text{FP})\,(\text{TN} \times \text{FN})}}. \tag{7}$$

F1-score is the harmonic mean of precision and recall. MCC is a balanced index that considers the TN. For these five metrics, precision and recall are complementary relationships. High precision value means lower commission error and high recall value means lower omission error. A high-performing CNN model is considered to be indicated by a high F1-score and MCC, with balanced precision and recall.

IV. RESULT AND ACCURACY ASSESSMENT

A. Experiment Setting

1) Construction of Dataset: Through data augmentation, we obtained 1656 samples for Iburi and 1056 samples for Jiuzhaigou, including both positive and negative samples. To ensure parity during experiments, the total number of samples in "known domains" (i.e., Iburi and Jiuzhaigou) was maintained at 1000 by way of random selection. A 7:3 ratio is applied to split the 1000 samples into training and testing datasets. Two benchmark models and three multidomain models were designed (see Table V) in accordance with the different proportional compositions of the training dataset samples. The initials indicate the abbreviation of the domains (Ib and J) and the following number indicates the sample number of the respective domains accounting for the entire training dataset (700, 200, 500, and 350).

2) Parameter Setting: The proposed network was implemented on the PyTorch framework as a backend on the Windows platform with a 4 GB GeForce RTX 3080 Laptop graphics card. A batch size of 5 was chosen, and an Adam optimizer was employed with an initial learning rate of 10^{-4}. The model with the lowest validation loss during the training process was chosen to validate the model's accuracy in the testing area.

B. Comparisons of Landslide Recognition Performance in Benchmark Model

To validate the improved performance of the proposed ResU-SENet over the classical ResU-Net, the Ib700 and J700 detectors were trained as benchmark detectors in Iburi and Jiuzhaigou, based on the ResU-Net and ResU-SENet models, respectively. Table VI details the results of the corresponding testing samples. Fig. 5 compares the robustness of ResU-Net and ResU-SENet for Iburi and Jiuzhaigou.

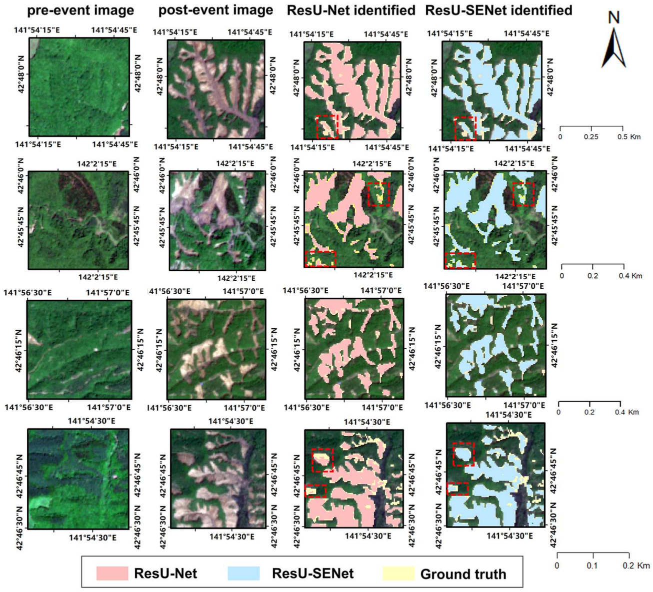

Fig. 6. Landslide identification results of trained ResU-Net and ResU-SENet on Iburi testing datasets. Red boxes show differences in results.

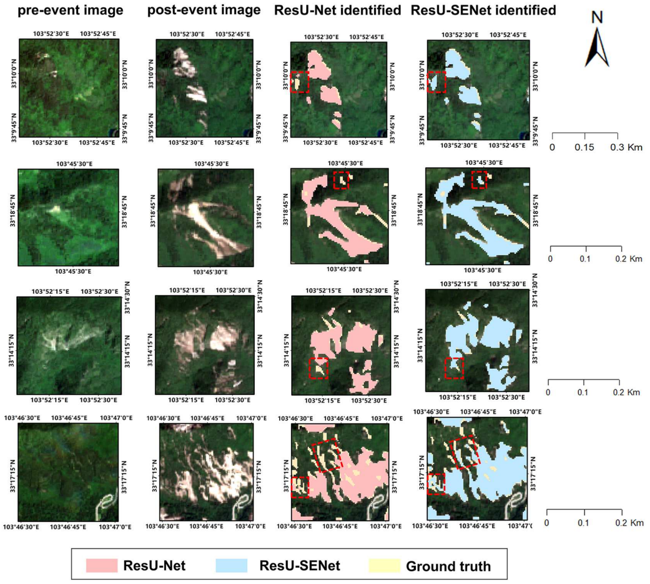

Fig. 7. Identification results of trained ResU-Net and ResU-SENet on Jiuzhaigou testing datasets. Red boxes show differences in results.

TABLE VII
LANDSLIDE IDENTIFICATION RESULTS OF DIFFERENT MODELS IN IBURI

Domain	Model	Detector	Precision	F1-score	Recall	MCC	IoU
Iburi	ResU-Net	Ib700	0.8936	0.8246	0.7775	0.7908	0.7073
		Ib500J200	0.8709	**0.8361**	**0.8165**	**0.7994**	**0.7219**
		Ib200J500	0.8897	0.7623	0.6863	0.7277	0.6212
		Ib350J350	0.8791	0.8219	0.7874	0.7867	0.7009
	ResU-SENet	Ib700	0.8766	0.853	0.8368	0.8175	0.746
		Ib500J200	0.8702	**0.8503**	**0.8403**	**0.8152**	**0.7432**
		Ib200J500	0.8808	0.7512	0.673	0.7159	0.6059
		Ib350J350	0.8711	0.8151	0.7894	0.7813	0.6924

The bold values represents better results compared to others.

TABLE VIII
LANDSLIDE IDENTIFICATION RESULTS OF DIFFERENT MODELS IN JIUZHAIGOU

Domain	Model	Detector	Precision	F1-score	Recall	MCC	IoU
Jiuzhaigou	ResU-Net	J700	0.8051	0.7532	0.719	0.7097	0.6085
		Ib500J200	0.8162	0.7254	0.6648	0.6844	0.5752
		Ib200J500	0.7919	**0.7968**	**0.7584**	**0.7254**	**0.6311**
		Ib350J350	0.8005	0.7567	0.7277	0.7121	0.6133
	ResU-SENet	J700	0.788	0.7876	0.7941	0.7449	0.6545
		Ib500J200	0.8075	0.7249	0.6708	0.6818	0.5744
		Ib200J500	0.7778	**0.7701**	**0.7742**	**0.7255**	**0.6304**
		Ib350J350	0.7869	0.7500	0.7319	0.7056	0.6037

The bold values represents better results compared to others.

The results show that the trained ResU-Net and ResU-SENet models achieve good performance in the Iburi and Jiuzhaigou datasets, which means that most landslides are correctly identified with high precision—in excess of 87.66% and 78.80%, respectively. Meanwhile, the proposed ResU-SENet outperforms ResU-Net in F1-score, Recall, MCC, and IoU metrics. Recall is notably increased by 5.93% and 7.51% for Iburi and Jiuzhaigou, and IoU is notably enhanced by 3.44% and 2.84%, respectively. Furthermore, the proposed ResUSENet retains a noticeable balance between precision and recall, with differences between the two indices of 3.98% and 0.61% for Iburi and Jiuzhaigou, respectively. Some of the landslide identification results for the Iburi and Jiuzhaigou testing datasets are shown in Figs. 6 and 7. It is observed that ResU-SENet captured some landslide details more accurately, with the majority of small-area landslides and ambiguous landslide boundary pixels being identified. This is also the reason for the significant improvements in recall and IoU.

C. Comparisons of Landslide Recognition Performance for Multidomain Model

The performance of three constructed multidomain models was compared against benchmark models for Iburi and Jiuzhaigou, respectively. Tables VII and VIII reveal the effect of sample proportion variation on landslide identification accuracy for Iburi and Jiuzhaigou, respectively. Using Table VII, we ranked the landslide identification performance of models in Iburi from highest to lowest for both ResU-Net and ResU-SENet: Ib500J200 $\geq$ Ib700 $>$ Ib350J350 $>$ Ib200J500. The landslide extraction capabilities of the Ib500J200 and Ib700 models are almost identical and, for the ResU-Net model, the accuracy metric of the Ib500J200 model is even slightly higher than that of the Ib700 model. Ib350J350 model achieved almost equal performance to Ib700 model based on ResU-Net. The Ib200J500 model exhibits the lowest performs, especially with the ResU-SENet model, with a 16.38% decrease in recall and a 0.1018 decrease in F1-score compared to the Ib700 model. We suspect that the insufficient number of Iburi samples caused the model to fail to fully learn the local environment characteristics.

From Table VIII, the performance of models for Jiuzhaigou, based on the ResU-Net model, was ranked from highest to lowest: Ib200J500 $>$ Ib350J350 $\geq$ J700 $>$ Ib500J200. Compared to the J700 model, the F1-score, MCC, recall, and IoU of the Ib200J500 model were improved by 0.0436, 0.0157, 3.94%, and 2.66%, respectively. For the ResU-SENet model, the performance of models from highest to lowest was

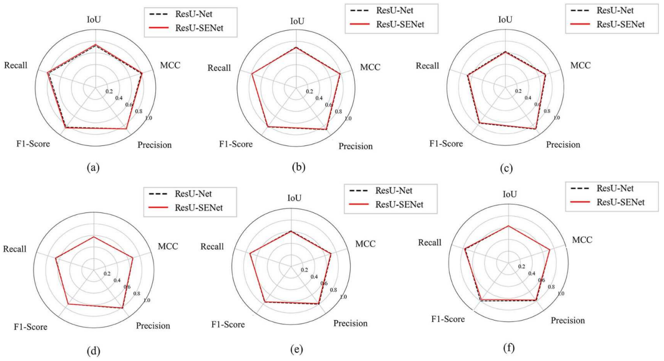

Fig. 8. Performance of ResU-Net and ResU-SENet models with different models in Jiuzhaigou and Iburi. First row shows results for Iburi area and second row shows results for Jiuzhaigou area. (a) and (d) Ib500J200 model. (b) and e) Ib350J350 model. (c) and (f) Ib200J500 model.

J700 > Ib200J500 > Ib350J350 > Ib500J200. The J700 benchmark model exhibited the highest landslide extraction performance. The Ib200J500 model exhibited a slightly inferior performance than the J700 model, with F1-score, MCC, recall, and IoU decreasing by 0.0175, 0.0194, 1.99%, and 2.41%, respectively. Recall of the Ib500J200 model decreased by 0.1233 compared with the J700 model, indicating an omission error due to the insufficient number of training samples for Jiuzhaigou.

To verify the effect of SE module embedding on the performance of the multidomain model, we compared the performance changes in the ResU-Net and ResU-SENet models based on different models, as shown in Fig. 8. Interestingly, from Fig. 8, we noted almost equal performance of ResU-Net and ResU-SENet in multidomain models, but no significant improvement in the two networks in a multidomain model.

Overall, we can conclude the following: 1) Sample mixing ratio determines the identification performance of the multidomain model. When testing the domain in which the corresponding training sample accounted for the dominant proportion in the multidomain model, the model gave a superior performance to the benchmark model—in other words, the Ib500J200 model outperforms the Ib700 model in Iburi while the Ib200J500 model outperforms the J700 model in Jiuzhaigou. Combining half the number of foreign domain samples (50%) with half of the local samples (50%) maintains almost the same identification performance as if trained entirely with local samples based on ResU-Net. 2) The overall landslide identification performance of the ResU-SENet embedded with the SE module in the multidomain model was not significantly improved. The effect of the sample on model performance was greater than the effect of model structure on model performance.

D. Model Generalization Performance

To test the generalization performance, the models trained in the above experiments were directly employed to predict landslides in a completely new geographic position (Palu), as well as some challenging scenes with different land cover types, landslide triggers, imaging models, and spatial distribution.

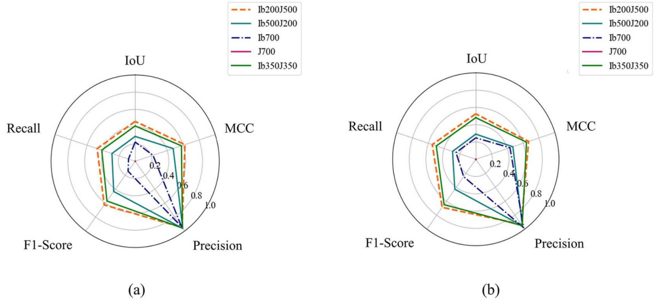

Fig. 9. Quantitative comparisons of accuracy in Palu. (a) Different models tested on ResU-Net. (b) Different models tested on ResU-SENet.

TABLE IX
LANDSLIDE IDENTIFICATION RESULTS OF DIFFERENT MODELS IN PALU

Domain	Model	Detector	Precision	F1-score	Recall	MCC	IoU
Palu	ResU−Net	J700	0.0066	0.0005	0.0003	-0.0434	0.0003
		H700	0.9381	0.1432	0.0831	0.2231	0.083
		Ib500J200	0.9618	0.4336	0.29	0.4755	0.2876
		Ib200J500	**0.9488**	**0.625**	**0.4751**	**0.6223**	**0.4613**
		Ib350J350	0.9566	0.5699	0.4177	0.5783	0.4088
	ResU−SENet	J700	0.0076	0.003	0.002	-0.1111	0.0015
		H700	0.9777	0.2483	0.2498	0.4324	0.2483
		Ib500J200	0.9536	0.4286	0.294	0.4687	0.2911
		Ib200J500	**0.9299**	**0.6875**	**0.5501**	**0.6677**	**0.526**
		Ib350J350	0.9493	0.6486	0.4993	0.6412	0.4815

The bold values represents better results compared to others.

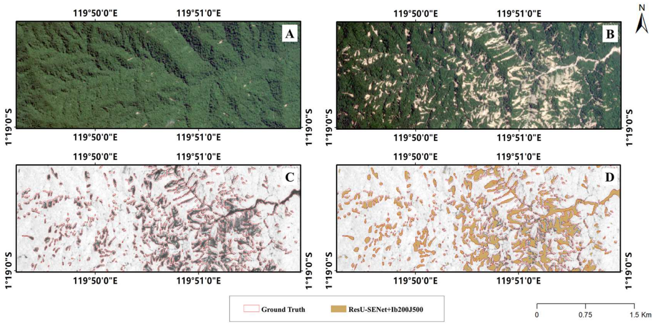

Fig. 10. Results of applying multidomain models to Palu. (a) Pre-event image. (b) Postevent image. (c) Ground truth. (d) Identification result of ResU-SENet with Ib200J500 model.

First, we predicted co-seismic landslide in Palu. From Fig. 9 and Table IX, we found that multidomain models exhibit significantly improved performance over the Ib700 and J700 models in Palu, with Ib200J500 models based on ResU-SENet showing the best performance, with an F1-score of 0.6875. Fig. 10 shows the landslide identification ability of Ib200J500 model in unknown domains.

Upon comparing the highest-performing multidomain model (Ib200J500) in the Palu region, based on the ResU-Net and ResU-SENet models, respectively, we can see from Fig. 11 that the ResU-SENet model with an embedded channel attention mechanism can improve model landslide identification performance to some extent.

Second, three challenging scenes were selected for landslide prediction. The Baige landslide was triggered by recurring rainfall, with the images captured in summer and autumn, respectively. The Big Sur landslide was triggered by loose soil and rock splitting and the images were obtained from Landsat 8.

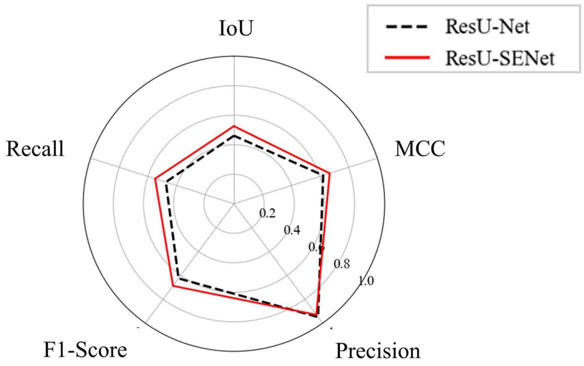

Fig. 11. Performance of Ib200J500 model based on ResU-Net and ResU-SENet models in Palu.

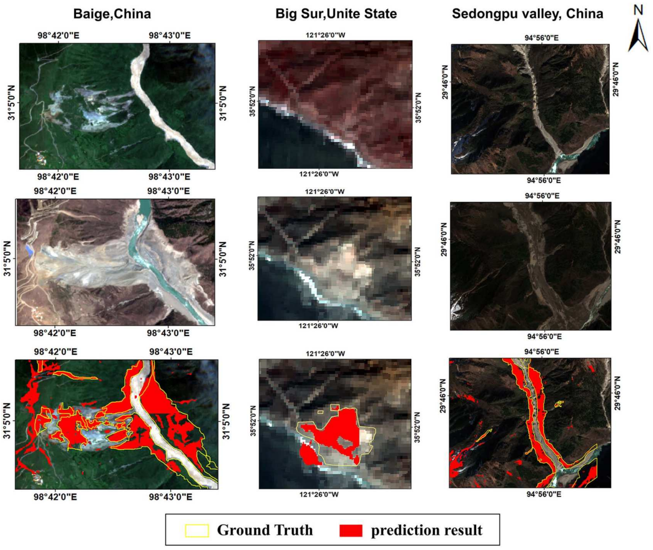

Fig. 12. Landslide identification result in challenging dataset. The first row is pre-event images, the second row is postevent images, and the third row is the identification results.

The Sedongpu valley landslide was triggered by rainfall and the images selected were from the winter season. The identification result of the Ib200J500 model based on ResU-SENet is shown in Fig. 12. The F1-score for the Baige, Big Sur, and Sedongpu landslides were 0.7247, 0.6709, and 0.6594, respectively.

At the same time, we found that model performance on unknown domains was biased toward higher precision and low recall, which was similar to observations from other DL studies undertaken within the field of multidomain learning and domain generalization [27], [47]. This means that areas identified as landslide areas can be trusted with high confidence; however, the inventory was not complete as it also omitted some landslides. This was not a poor result as it accurately mapped landslides without any prior training in this particular area. An algorithm that can rapidly generate the first map of landslide distribution would be of immense value to decision-makers when planning relief operations.

TABLE X
LANDSLIDE IDENTIFICATION RESULT COMPARED WITH OTHER MODELS

Domain	Traind model	Network	precision	F1	recall	MCC	IoU
Iburi	Ib700	CGNet [47]	0.6229	0.6199	0.6356	0.5309	0.4550
		LANet [48]	0.7821	0.7840	0.7897	0.7287	0.6463
		MACU-Net [49]	0.8392	0.8323	0.8295	0.7902	0.7152
		ResU-Net [27]	0.8926	0.8246	0.7775	0.7908	0.7073
		ResU-SENet	**0.8766**	**0.853**	**0.8368**	**0.8175**	**0.7460**
Jzg	J700	CGNet [47]	0.6942	0.6701	0. 5922	0.5700	0.4683
		LANet [48]	0.696	0.7029	0.7134	0.6807	0.5667
		MACU-Net [49]	0.7612	0.7441	0.7356	0.6939	0.5908
		ResU-Net [27]	0.8051	0.7532	0.719	0.7097	0.6085
		ResU-SENet	**0.7880**	**0.7876**	**0.7941**	**0.7449**	**0.6545**

The bold values represents better results compared to others.

V. DISCUSSION

A. *Advantages of Proposed ResU-SENet*

We obtained satisfactory landslide identification results for Iburi and Jiuzhaigou using freely accessible Sentinel-2 images and DEM data. Compared with previous work [31], [48], [49], our method has greater potential in co-seismic landslide inventory mapping. Specifically, it is noted that our approach achieved an F1-score of 0.7876 in the Jiuzhaigou study area with the J700 model based on ResU-SENet and that Yi and Zhang [50] achieved 0.7650 using RapidEye images with spatial resolution of 5 m. In Iburi, the Ib700 model based on ResU-SENet obtained an F1-score of 0.8530 while Zhang et al. [51] obtained 0.8288 using Planet Satellite images with a spatial resolution of 3 m. This further demonstrates that our model performs well under medium-resolution images. By comparing with several state-of-the-art semantic segmentation model, including CGNet [52], LANet [53], and MACU-Net [54], our proposed ResU-SENet performs best both the Iburi and Jiuzhaigou dataset as presented in Table X. LANet, MACU-Net, and ResU-Net were overall higher than CGNet in all metrics. This is likely due to the fact that CGNet is a light-weight model with less than 2 M parameters.

Gradient-weighted class activation mapping uses the gradients of particular classes flowing into the final layer to generate an attention map that highlights the important regions in predicting that class [55]. We selected some of the landslide samples from Jiuzhaigou and Iburi and visualized the last feature maps predicted by CGNet, LANet, MACU-Net, ResU-Net, and ResU-SENet for comparison. As shown in Fig. 13, the landslide areas were precisely located using the MACU-Net, ResU-SENet, and ResU-Net. Heat value shows a spatial gradient descent from the landslides focus to the edge and background. The heat value of landslides based on ResU-SENet is more intense and focused than other models, further indicating the superior performance of ResU-SENet in landslide identification.

The reason why this study has focused on the channel attention mechanism without considering the spatial attention mechanism is that the original semantic segmentation network is well-focused on spatial information and can realize the extraction of landslide spatial information [56]. We conducted experiments integrating the Convolutional Block Attention Module (CBAM) [57] into ResU-Net, which focuses on both channel

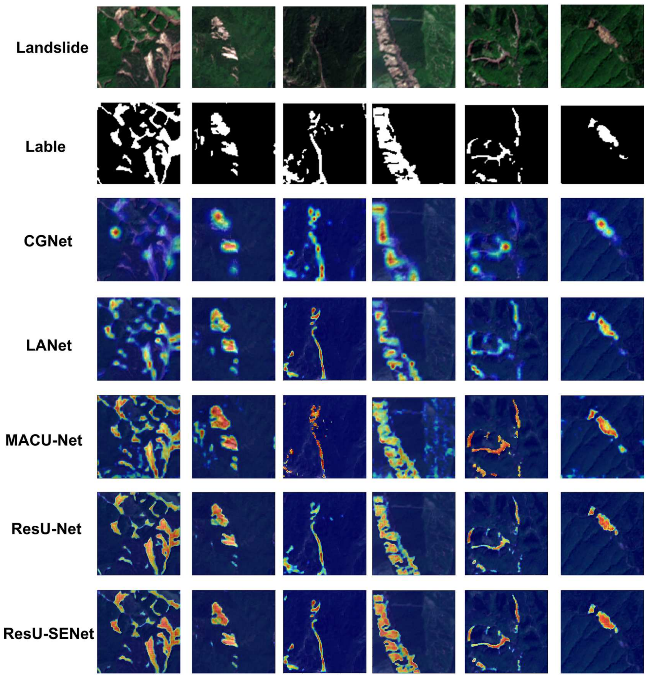

Fig. 13. Heatmaps for landslide samples.

and spatial two dimensions. Unsurprisingly, ResU-Net embedded with CBAM showed no significant improvement in accuracy compared to ResU-SENet. Considering the efficiency and complexity of the model, we selected ResU-SENet for landslide identification.

We found that overall landslide extraction accuracy in Jiuzhaigou to be lower than that of Iburi. In Iburi, landslide areas account for 5% of the total study area while, in Jiuzhaigou, landslide areas occupy 1.5% of the entire study area. This small volume of positive samples makes training the landslide identification model in Jiuzhaigou more difficult.

B. Advantages of Constructing Multidomain Models

We proposed the idea of replacing the mostly local domain annotated samples with foreign domain annotated samples to construct multidomain models. Under such conditions, if the multidomain models could maintain comparable, or even excessive, landslide extraction capabilities to the benchmark model, it would substantially reduce the number of samples and effort required to annotate new labels in new co-seismic areas.

Three attempts were made at the sample mixing ratio of the local domain and foreign domain: 1:6, 2:5, and 1:1. When the substitution number of foreign domains was 600, the landslide model performance dropped significantly in the local domain. F1-scores were 0.2341 and 0.3929 when applying the Ib100J600 and Ib600J100 models on Iburi and Jiuzhaigou, respectively. As the extraction accuracy was poor, we did not mention this ratio above. When the substitution number of foreign domains was 500, the performance was slightly inferior to that of the benchmark model (i.e., Ib700 and J700), but is a noticeable improvement compared to 6:1. Performance was almost equal to the benchmark model when the ratio of samples was half for each of the two regions. This potentially indicates that, when the substitution ratio is appropriate, the model can better learn different landslide characteristics, topographic environments, imaging conditions, and illumination conditions.

It is estimated that an average of 30 s is required to label a landslide in an RS image. In other words, for domains with a large number of landslides, such as Iburi, if half of the samples from the Iburi domain were replaced with samples from the foreign domain where landslide-annotated samples already exist, and the equal identification performance was maintained as if trained entirely with Iburi samples, ∼30 hours would be saved. It should be noted that this is only for one area of landslide inventory mapping. We believe that the multidomain models will be hugely practical in landslide emergency disasters.

In addition, the experiment showed the landslide extraction capacity of ResU-Net and ResU-SENet in Iburi and Jiuzhaigou to be almost equal in multidomain models. As shown in Fig. 8(a)–(f), their evaluation metrics almost overlap. In this case, we believe that training data is more important than the models. Multidomain models substitute half (50%) or even more (72%) of training samples in the local domain with foreign domain samples, implying the lack of local domain training samples in DL. Therefore, the results are identical for both models. It is worth mentioning that adding a small number of foreign domain samples to the local domain model could enhance the landslide identification result in the local domain. It seems that including a certain number of foreign samples exerts a positive impact because it increases the diversity of samples.

C. Relationship Between Model Generalization and Data Distribution

In this subsection, we mainly discussed the difficulty of model generalization and the connection between model generalization and data distribution.

First, landslide exhibits notable variation in images, resulting in a high intraclass variance across geographical regions [23]. Fig. 14(a) shows several landslide samples from the study area with different shapes, hues, and land cover types. Second, the change detection of co-seismic landslides is also influenced by other change scenarios, including illumination, the season of image acquisition, and land cover changes that are similar to landslides. We select several samples from our study areas, of which Fig. 14(b) shows the changes from woodland or cultivated land to bare land and seasonal variations. Third, by comparing the DEM of different cases, it can be found that there are obvious topographical differences [see Fig. 14(c)]. For an island like Iburi, the elevation ranges from 635 to 0 m, whereas for Jiuzhaigou, located in southwest China, the corresponding average elevation is 3295.9 m. These all pose significant challenges for model generalization ability.

In the experiment of model generalization performance, the Ib200J500 model performs best in the experiments at Palu, potentially indicating that the Ib200J500 model data distribution is more similar to Palu. Maximum mean discrepancy (MMD) is often used to measure the similarity or variability of data distribution between two domains [58]. We suppose that there exists source data satisfying the distribution $X^{(s)}$ and target data satisfying the distribution $X^{(t)}$, H denotes the reproducing

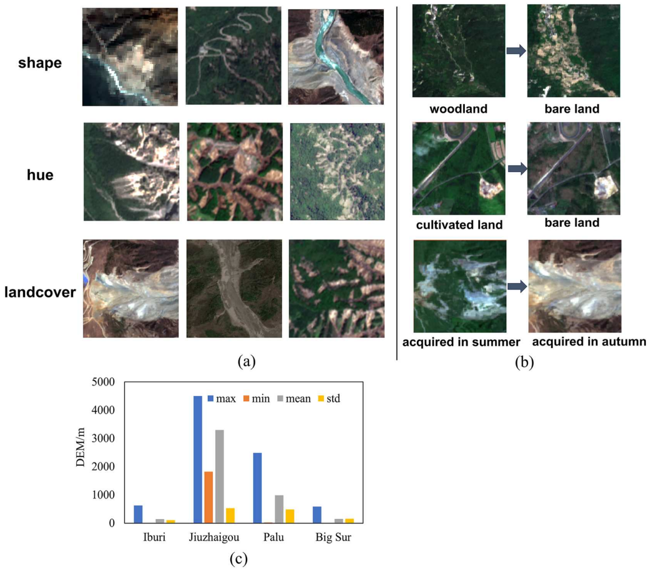

Fig. 14. Challenges of co-seismic landslide identification. (a) Differences in landslide samples from different study areas. (b) Effects of land cover change and seasonal variation on landslide change detection. (c) Comparison of DEM in different study areas.

TABLE XI
RESULTS OF MMD BETWEEN PALU AND TRAINED MODELS

	pre NDVI	post NDVI	pre B2	pre B3	pre B4	post B2	post B3	post B4	slope	hillshade
Ib200J500	**0.2497**	0.4711	**0.9607**	**0.4291**	**0.2318**	0.5905	0.3883	**0.1147**	**0.2203**	**0.1054**
Ib350J350	0.314	0.5841	1.0275	0.9493	0.4285	0.3284	**0.3186**	0.1439	0.2865	0.1709
Ib500J200	0.3706	0.6324	1.3434	1.6547	0.5818	**0.2549**	0.4151	0.2248	0.4996	0.241
Ib700	1.6853	0.3453	1.7954	2.7623	0.6115	0.4804	0.901	0.2492	0.7987	0.3004
J700	0.3319	**0.0982**	1.6621	0.1737	0.1212	1.4611	0.9589	0.252	0.4783	0.1336

The bold values represents better results compared to others.

kernel Hilbert space (RKHS) and ∅ (·): X→H denotes the nonlinear feature mapping function of the original feature space mapped to RKHS. $X^{(s)}$ and $X^{(t)}$ in the MMD of RKHS can be expressed as

$$D_{\text{MMD}} = \| \frac{1}{N} \sum_{i=1}^{N} \emptyset \left(X^{(s)} \right) - \frac{1}{M} \sum_{i=1}^{M} \emptyset \left(X^{(t)} \right) \|_{H} . \quad (8)$$

If the distributions of two domains tend to be identical and the RKHS is universal, MMD tends to be 0. This also means that the model could have an ideal generalization performance in the unknown domain. In this study, we directly use the models constructed from the Iburi and Jiuzhaigou samples as the source domain and from the Palu samples as the target domain, and take the bands corresponding to each region as input. The results of MMD between different models and Palu are shown in Table XI.

We can see from the calculated results in Table XI that the MMD value between the Ib200J500 model and Palu samples achieves minimum values, with the exception of post-NDVI, post-B2, and post-B3 bands. This is also consistent with our experimental result that Ib200J500 performs better in Palu. In summary, the model generalization performance is strongly related to the similarity between the source data distribution and target data distribution. In the landslide identification task of the unknown domains, calculating the MMD could provide a guideline for the model selection.

TABLE XII
RESULTS OF MMD

	pre NDVI	post NDVI	pre B2	pre B3	pre B4	post B2	post B3	post B4	slope	hillshade
Ib to Ld	**0.6417**	**0.6452**	**1.5966**	**1.1134**	**0.7317**	**0.52**	**0.4775**	1.2634	1.7478	0.9764
J to Ld	2.3799	0.7867	1.8563	2.3926	0.8136	1.4534	0.7339	0.2357	0.3884	0.1524

The bold values represents better results compared to others.

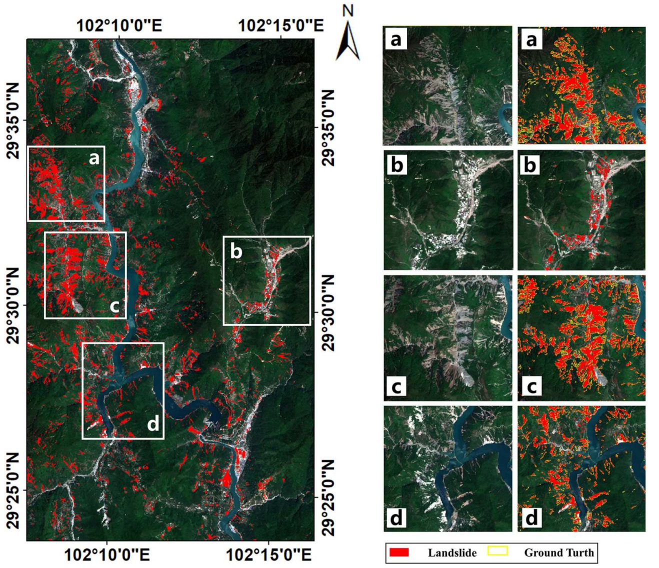

Fig. 15. Landslide identification results generated by Ib700 model based on ResU-SENet.

D. *Utilizing Data Distribution Differences to Guide Luding Earthquake Landslide Mapping*

On September 5, 2022, an Ms 6.8 earthquake struck Luding County, Ganzi Prefecture, Sichuan Province, China.

We first acquired Sentinel-2 images and DEM based on the GEE platform. Then, 4103 co-seismic landslides covering an area of 589 km^2 were interpreted to obtain a landslide mask of the Luding area, by using the pre- and postevent Sentinel-2 images and Google Earth high-resolution images.

Considering the close geographic location and similar topographical features between Jiuzhaigou and Luding, the model trained in Jiuzhaigou was indiscriminately used to predict landslides in LD. However, to validate the observation that data distribution affects the model generalization ability proposed in this study, the MMD was also calculated. Table XII shows that the data distributions from Iburi and LD are more similar than those of Jiuzaigou and LD. Therefore, the Ib500J200 and Ib700 models were applied to landslide identification in Luding.

We found that the performance of the Ib700 model based on ResU-SENet obtained a recall of 68.09% and an F1-score of 0.7433 and performed best. The Ib500J200 model based on ResU-SENet obtained a recall of 70.23% and an F1-score of 0.6741.

Fig. 15 presents the landslide identification results generated by Ib700 model based on ResU-SENet for the Luding area. From the four subregions (marked as a–d) in Fig. 15, we found most mountain landslides were correctly identified. Compared with previous work, Dai et al. [59] employed an autonomous aerial vehicle and GF-6 remote sensing images for co-seismic landslide identification in Moxi Town, Luding County and obtained an F1-score of 0.83 and recall of 79.8%. Our results are still comparable, as well as it being based on free-access medium-resolution RS images.

E. Limitations and Future Study

In this work, we perform landslide identification utilizing multichannel datasets based on DL method. We emphasized the importance of each band for the occurrence of landslides through the SE channel-wise attention mechanism but did not obtain specific weight values. Therefore, in the future, we will focus on the interpretability of the model. In the experiment of comparisons of landslide recognition performance for multidomain model, the sample substitution ratio is not strictly chosen, the relationship between the substitution ratio and the model performance will be further investigated.

VI. CONCLUSION

This article presents a generalized deep-learning-based method for the rapid mapping of co-seismic landslides, utilizing freely accessible Sentinel-2 images and DEM. The process of generating landslide training samples based on the GEE cloud platform and ArcGIS platform was proposed and multichannel landslide datasets of four study areas were created. Considering the contribution of channels to the occurrence of landslide was different, a new semantic segmentation model called ResU-SENet was proposed. It could adaptively adapt the weights of each band and outperform the CGNet, LANet, MACU-Net, and ResU-Net.

Confronted with the problem that when a deep neural network performs the landslide extraction task from a new domain or data distribution, its performance will be greatly reduced. We utilize multidomain learning to improve the model generalization ability. From the experimental results, the multidomain Ib350J350 model almost maintains identification performance at the level achievable if trained entirely with local sample models (Ib700 and J700 models). This finding potentially reduces the number of new training samples required by 50%. Meanwhile, we found that when testing domains where the corresponding training sample accounts for a dominant proportion with the multidomain model, the model outperforms the benchmark model. For instance, when employing the Ib500J200 model to identify landslides in Iburi, the result bettered that of the Ib700 model. Hence, adding a small number of foreign domain samples is equal to data augmentation. Applying models trained by Iburi and Jiuzhaigou samples directly to completely unknown domains, F1-score reached 0.6875 in Palu, which implies the good generalization capability of our model. Notably, by analyzing the connection between model generalization and data distribution, the Ib700 model trained on ResU-SENet achieved an F1-score of 0.7433 for the Luding co-seismic landslide identification application. The calculation of MMD provides a guideline for the model selection.

A co-seismic landslide extraction model with generalization ability solves the key bottleneck in landslide emergency mapping. Further research will combine GEE or Google AI online platforms to provide favorable support for rapid co-seismic landslide mapping in unknown domains.

REFERENCES

[1] D. K. Keefer, “Landslides caused by earthquakes,” *Geological Soc. Amer. Bull.*, vol. 95, no. 4, pp. 406–421, Apr. 1984, doi: 10.1130/0016-7606(1984)95<406: LCBE>2.0.CO;2.

[2] C. Xu, X. Xu, B. Zhou, and L. Shen, “Probability of coseismic landslides: A new generation of earthquake-triggered landslide hazard model,” *J. Eng. Geol.*, vol. 27, no. 5, pp. 1122–1130, Sep. 2019, doi: 10.13544/j.cnki.jeg.2019084.

[3] A. Roccati, G. Paliaga, F. Luino, F. Faccini, and L. Turconi, “GIS-based landslide susceptibility mapping for land use planning and risk assessment,” *Land*, vol. 10, no. 2, Feb. 2021, Art. no. 162, doi: 10, 162. 10.3390/land10020162.

[4] E. L. Harp, D. K. Keefer, H. P. Sato, and H. Yagi, “Landslide inventories: The essential part of seismic landslide hazard analyses,” *Eng. Geol.*, vol. 122, no. 1/2, pp. 9–21, Sep. 2011, doi: 10.1016/j.enggeo.2010.06.013.

[5] P. Lu, Y. Qin, Z. Li, A. C. Mondini, and N. Casagli, “Landslide mapping from multi-sensor data through improved change detection-based Markov random field,” *Remote Sens. Environ.*, vol. 321, Sep. 2019, Art. no. 111235, doi: 10.1016/j.rse.2019.111235.

[6] Z. Li, W. Shi, S. W. Myint, P. Lu, and Q. Wang, “Semi-automated landslide inventory mapping from bitemporal aerial photographs using change detection and level set method,” *Remote Sens. Environ.*, vol. 175, pp. 214–230, Jan. 2016, doi: 10.1016/j.rse.2016.01.003.

[7] A. C. Mondini, K.-T. Chang, and H.-Y. Yin, “Combining multiple change detection indices for mapping landslides triggered by typhoons,” *Geomorphology*, vol. 134, no. 3/4, pp. 440–451, Feb. 2011, doi: 10.1016/J.GEOMORPH.2011.07.021.

[8] R. Parker et al., “Mass wasting triggered by the 2008 Wenchuan earthquake is greater than orogenic growth,” *Nat. Geosci.*, vol. 4, no. 7, pp. 449–452, May 2011, doi: 10.1038/NGEO1154.

[9] M. I. Sameen and B. Pradhan, “Landslide detection using residual networks and the fusion of spectral and topographic information,” *IEEE Access*, vol. 7, pp. 114363–114373, 2019, doi: 10.1109/ACCESS.2019.2935761.

[10] R. Behling, S. Roessner, H. Kaufmann, and B. Kleinschmit, “Automated spatiotemporal landslide mapping over large areas using rapid eye time series data,” *Remote Sens.*, vol. 6, no. 9, pp. 8026–8055, Aug. 2014, doi: 10.3390/rs6098026.

[11] F. Guzzetti, A. C. Mondini, M. Cardinali, F. Fiorucci, M. Santangelo, and K.-T. Chang, “Landslide inventory maps: New tools for an old problem,” *Earth Sci. Rev.*, vol. 112, no. 1–2, pp. 42–66, Apr. 2012, doi: 10.3390/rs6098026.

[12] S. W. Myint, P. Gober, A. Brazel, S. Grossman-Clarke, and Q. Weng, “Per-pixel vs. object-based classification of urban land cover extraction using high spatial resolution imagery,” *Remote Sens. Environ.*, vol. 115, no. 5, pp. 1145–1161, May 2011, doi: 10.1016/J.RSE.2010.12.017.

[13] J. Long, E. Shelhamer, and T. Darrell, “Fully convolutional networks for semantic segmentation,” in *Proc. IEEE Conf. Comput. Vis. Pattern Recognit.*, 2015, pp. 640–651.

[14] X. Gao, T. Chen, R. Niu, and A. Plaza, “Recognition and mapping of landslide using a fully convolutional DenseNet and influencing factors,” *IEEE J. Sel. Topics Appl. Earth Observ. Remote Sens.*, vol. 14, pp. 7881–7894, 2021, doi: 10.1109/JSTARS.2021.3101203.

[15] O. Ronneberger, P. Fischer, and T. Brox, “U-Net: Convolutional networks for biomedical image segmentation,” in *Proc. Med. Image Comput. Comput.-Assist. Interv.*, 2015, pp. 234–241.

[16] V. Badrinarayanan, A. Kendall, and R. Cipolla, “SegNet: A deep convolutional encoder-decoder architecture for image segmentation,” *IEEE Trans. Pattern Anal. Mach. Intell.*, vol. 39, no. 12, pp. 2481–2495, Dec. 2017, doi: 10.1109/TPAMI.2016.2644615.

[17] L.-C. Chen, G. Papandreou, I. Kokkinos, K. Murphy, and A. L. Yuille, “DeepLab: Semantic image segmentation with deep convolutional nets, atrous convolution, and fully connected CRFs,” *IEEE Trans. Pattern Anal. Mach. Intell.*, vol. 40, no. 4, pp. 834–848, Apr. 2018, doi: 10.1109/TPAMI.2017.2699184.

[18] J. Liu et al., "Image recognition of co-seismic landsldie based on GEE and U-net neural network," *J. Geo-Inf. Sci.*, vol. 24, no. 7, pp. 1275–1285, Nov. 2021, doi: 10.12082/dqxxkx.2022.210704.

[19] B. Yu, F. Chen, C. Xu, L. Wang, and N. Wang, "Matrix SegNet: A practical deep learning framework for landslide mapping from images of different areas with different spatial resolutions," *Remote Sens.*, vol. 13, no. 16, Nov. 2021, Art. no. 3158, doi: 10.3390/rs13163158.

[20] W. Lu, Y. Hu, Z. Zhang, and W. Cao, "A dual-encoder U-Net for landslide detection using Sentinel-2 and DEM data," *Landslides*, vol. 20, pp. 1975–1987, Jun. 2023, doi: 10.1007/s10346-023-02089-5.

[21] Z. Zhang, Q. Liu, and Y. Wang, "Road extraction by deep residual U-Net," *IEEE Geosci. Remote Sens. Lett.*, vol. 20, pp. 749–753, May 2018, doi: 10.1109/LGRS.2018.2802944.

[22] D. Peng, H. Guan, Y. Zang, and L. Bruzzone, "Full-level domain adaptation for building extraction in very-high-resolution optical remote-sensing images," *IEEE Trans. Geosci. Remote Sens.*, vol. 60, 2022, Art. no. 5607317, doi: 10.1109/TGRS.2021.3093004.

[23] Q. Xu, C. Ouyang, T. Jiang, X. Yuan, X. Fan, and D. Cheng, "MFFENet and ADANet: A robust deep transfer learning method and its application in high precision and fast cross-scene recognition of earthquake-induced landslides," *Landslides*, vol. 19, pp. 1617–1647, Mar. 2022, doi: 10.1007/s10346-022-01847-1.

[24] X. Zhang, W. Yu, M.-O. Pun, and W. Shi, "Cross-domain landslide mapping from large-scale remote sensing images using prototype-guided domain-aware progressive representation learning," *ISPRS J. Photogram. Remote Sens.*, vol. 197, pp. 1–17, Jan. 2023, doi: 10.1016/j.isprsjprs.2023.01.018.

[25] S. Qin et al., "Landslide detection from open satellite imagery using distant domain transfer learning," *Remote Sens.*, vol. 13, no. 17, Aug. 2021, Art. no. 3383, doi: 10.3390/rs13173383.

[26] S. R. Meena et al., "HR-GLDD: A globally distributed dataset using generalized deep learning (DL) for rapid landslide mapping on high-resolution (HR) satellite imagery," *Earth Syst. Sci. Data*, vol. 15, no. 7, pp. 3283–3298, Jul. 2023, doi: 10.5194/essd-15-3283-2023.

[27] N. Prakash, A. Manconi, and S. Loew, "A new strategy to map landslides with a generalized convolutional neural network," *Sci. Rep.*, vol. 11, no. 1, Art. no. 9722, May 2021, doi: 10.1038/s41598-021-89015-8.

[28] H. Yamagishi and F. Yamazaki, "Landslides by the 2018 Hokkaido Iburi-Tobu Earthquake on September 6," *Landslides*, vol. 15, no. 12, pp. 2521–2524, Oct. 2018, doi: 10.1007/s10346-018-1092-z.

[29] F. Wang et al., "Coseismic landslides triggered by the 2018 Hokkaido, Japan (Mw 6.6), earthquake: Spatial distribution, controlling factors, and possible failure mechanism," *Landslides*, vol. 16, no. 8, pp. 1551–1566, May 2019, doi: 10.1007/s10346-019-01187-7.

[30] X. Fan et al., "Coseismic landslides triggered by the 8th August 2017 Ms 7.0 Jiuzhaigou earthquake (Sichuan, China): Factors controlling their spatial distribution and implications for the seismogenic blind fault identification," *Landslides*, vol. 15, no. 5, pp. 967–983, Feb. 2018, doi: 10.1007/s10346-018-0960-x.

[31] X. Wang, X. Fan, Q. Xu, and P. Du, "Change detection-based co-seismic landslide mapping through extended morphological profiles and ensemble strategy," *ISPRS J. Photogram. Remote Sens.*, vol. 187, pp. 225–239, May 2022, doi: 10.1016/j.isprsjprs.2022.03.011.

[32] Y. Tian, C. Xu, S. Ma, X. Xu, S. Wang, and H. Zhang, "Inventory and spatial distribution of landslides triggered by the 8th August 2017 MW 6.5 Jiuzhaigou earthquake, China," *J. Earth Sci.*, vol. 30, no. 1, pp. 206–217, Feb. 2019, doi: 10.1007/s12583-018-0869-2.

[33] H. Bao et al., "Early and persistent supershear rupture of the 2018 magnitude 7.5 Palu earthquake," *Nat. Geosci.*, vol. 12, no. 3, pp. 200–205, Feb. 2019, doi: 10.1038/s41561-018-0297-z.

[34] H. Tanyas, D. Kirschbaum, T. Gorum, C. J. van Westen, and L. Lombardo, "New insight into post-seismic landslide evolution," *Front. Earth Sci.*, vol. 9, Jul. 2021, Art. no. 700546, doi: 10.3389/feart.2021.700546.

[35] S. R. Meena et al., "Rapid mapping of landslides in the Western Ghats (India) triggered by 2018 extreme monsoon rainfall using a deep learning approach," *Landslides*, vol. 18, no. 5, pp. 1937–1950, Jan. 2021, doi: 10.1007/s10346-020-01602-4.

[36] M. Van Den Eeckhaut et al., "The effectiveness of hillshade maps and expert knowledge in mapping old deep-seated landslides," *Geomorphology*, vol. 67, no. 3/4, pp. 351–363, Apr. 2005, doi: 10.1016/j.geomorph.2004.11.001.

[37] Y. Alimohammadlou, B. F. Tanyu, A. Abbaspour, and P. L. Delamater, "Automated landslide detection model to delineate the extent of existing landslides," *Nat. Hazards*, vol. 107, no. 2, pp. 1639–1656, Mar. 2021, doi: 10.1007/s11069-021-04650-8.

[38] N. Gorelick, M. Hancher, M. Dixon, S. Ilyushchenko, D. Thau, and R. Moore, "Google Earth Engine: Planetary-scale geospatial analysis for everyone," *Remote Sens. Environ.*, vol. 202, pp. 18–27, Dec. 2017, doi: 10.1016/j.rse.2017.06.031.

[39] W. Huang et al., "An efficient user-friendly integration tool for landslide susceptibility mapping based on support vector machines: SVM-LSM toolbox," *Remote Sens.*, vol. 14, no. 14, Jul. 2022, Art. no. 3408, doi: 10.3390/rs14143408.

[40] S. Jia, S. Jiang, Z. Lin, N. Li, M. Xu, and S. Yu, "A survey: Deep learning for hyperspectral image classification with few labeled samples," *Neurocomputing*, vol. 448, pp. 179–204, Aug. 2021, doi: 10.1016/j.neucom.2021.03.035.

[41] C. Shorten and T. M.Khoshgoftaar, "A survey on image data augmentation for deep learning," *J. Big Data*, vol. 6, no. 1, pp. 1–48, Jul. 2019, doi: 10.1186/s40537-019-0197-0.

[42] J. Kukačka, V. Golkov, and D. Cremers, "Regularization for deep learning: A taxonomy," 2017, doi: 10.48550/arXiv.1710.10686.

[43] J. Hu, L. Shen, and G. Sun, "Squeeze-and-excitation networks," in *Proc. IEEE Conf. Comput. Vis. Pattern Recognit.*, 2018, pp. 7132–7141.

[44] K. He, X. Zhang, S. Ren, and J. Sun, "Identity mappings in deep residual networks," in *Proc. Eur. Conf. Comput. Vis.*, 2016, pp. 630–645.

[45] F. Milletari, N. Navab, and S.-A. Ahmadi, "V-Net: Fully convolutional neural networks for volumetric medical image segmentation," in *Proc. 4th Int. Conf. 3D Vis.*, 2016, pp. 565–571.

[46] S. V. Stehman, "Selecting and interpreting measures of thematic classification accuracy," *Remote Sens. Environ.*, vol. 62, no. 1, pp. 77–89, Oct. 1997, doi: 10.1016/S0034-4257(97)00083-7.

[47] O. Ghorbanzadeh, A. Crivellari, P. Ghamisi, H. Shahabi, and T. Blaschke, "A comprehensive transferability evaluation of U-Net and ResU-Net for landslide detection from Sentinel-2 data (case study areas from Taiwan, China, and Japan)," *Sci. Rep.*, vol. 11, no. 1, pp. 1–20, Jul. 2021, doi: 10.1038/s41598-021-94190-9.

[48] P. Liu, Y. Wei, Q. Wang, Y. Chen, and J. Xie, "Research on post-earthquake landslide extraction algorithm based on improved U-Net model," *Remote Sens.*, vol. 12, no. 5, Mar. 2020, Art. no. 894, doi: 10.3390/rs12050894.

[49] Z. Yang, C. Xu, and L. Li, "Landslide detection based on ResU-Net with transformer and CBAM embedded: Two examples with geologically different environments," *Remote Sens.*, vol. 14, no. 12, Jun. 2022, Art. no. 2885, doi: 10.3390/rs14122885.

[50] Y. Yi and W. Zhang, "A new deep-learning-based approach for earthquake-triggered landslide detection from single-temporal rapideye satellite imagery," *IEEE J. Sel. Topics Appl. Earth Observ. Remote Sens.*, vol. 13, pp. 6166–6176, 2020, doi: 10.1109/JSTARS.2020.3028855.

[51] P. Zhang, C. Xu, M. A. S., X. Shao, Y. Tian, and B. Wen, "Automatic extraction of seismic landslides in large areas with complex environments based on deep learning: An example of the 2018 Iburi earthquake, Japan," *Remote Sens.*, vol. 12, no. 23, Oct. 2020, Art. no. 3992, doi: 10.3390/rs12233992.

[52] Z. Zhang and Y. Pang, "CGNet: Cross-guidance network for semantic segmentation," *Sci. China Inf. Sci.*, vol. 63, Jan. 2020, Art. no. 120104, doi: 10.1007/s11432-019-2718-7.

[53] L. Ding, H. Tang, and L. Bruzzone, "LANet: Local attention embedding to improve the semantic segmentation of remote sensing images," *IEEE Trans. Geosci.*, vol. 59, no. 1, pp. 426–435, Jan. 2021, doi: 10.1109/TGRS.2020.2994150.

[54] R. Li, C. Duan, S. Zheng, C. Zhang, and P. M. Atkinson, "MACU-Net for semantic segmentation of fine-resolution remotely sensed images," *IEEE Geosci. Remote Sens. Lett.*, vol. 19, 2022, Art. no. 8007205, doi: 10.1109/LGRS.2021.3052886.

[55] R. R. Selvaraju, M. Cogswell, A. Das, R. Vedantam, D. Parikh, and D. Batra, "Grad-CAM: Visual explanations from deep networks via gradient-based localization," in *Proc. IEEE Int. Conf. Comput. Vis.*, 2017, pp. 618–626.

[56] O. Ghorbanzadeh, K. Gholamnia, and P. Ghamisi, "The application of ResU-net and OBIA for landslide detection from multi-temporal Sentinel-2 images," *Big Earth Data*, vol. 7, no. 4, pp. 961–985, Feb. 2022, doi: 10.1080/20964471.2022.2031544.

[57] S. Woo, J. Park, L. J-Y., and I. S. Kweon, "CBAM: Convolutional block attention module," in *Proc. Eur. Conf. Comput. Vis.*, 2018, pp. 3–19.

[58] K. M. Borgwardt, A. Gretton, M. J. Rasch, H.-P. Kriegel, B. Schölkopf, and A. J. Smola, "Integrating structured biological data by kernel maximum mean discrepancy," *Bioinformatics*, vol. 22, no. 14, pp. e49–e57, Jul. 2006, doi: 10.1093/bioinformatics/btl242.

[59] L. Dai et al., "Coseismic landslides triggered by the 2022 luding Ms6. 8 earthquake, China," *Landslides*, vol. 20, no. 6, pp. 1277–1292, Apr. 2023, doi: 10.1007/s10346-023-02061-3.

Jing Yang received the B.S. degree and the M.Sc. degree in photogrammetry and remote sensing from the Chang'an University, Xi'an, China, in 2010 and 2023.

She is currently a teaching assistant with the Qinghai University of Technology, Xining, China. Her research interest includes interpretation of remote sensing images, deep learning, and landslide detection.

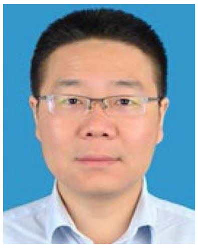

Mingtao Ding (Member, IEEE) received the B.S. and Ph.D. degrees in applied mathematics from the Northwestern Polytechnical University, Xi'an, China, in 2007 and 2010, respectively.

From 2011 to 2012, he was a Post-Doctoral Fellow with the Department of Electrical and Computer Engineering, Duke University, Durham, NC, USA. In 2013, he joined the College of Geological Engineering and Geomatics, Chang'an University, Xi'an, China, where he is currently an Associated Professor in remote sensing science and technology. He specializes in machine learning, artificial intelligence, and applied statistics. His research interests include landslide detection, mapping, and monitoring with interferometric synthetic aperture radar and multispectral remote sensing.

Wubiao Huang received the B.Sc. degree in geomatics engineering from the Xiamen University of technology, Xiamen, China, in 2020, and the M.Sc. degree in photogrammetry and remote sensing from the Chang'an University, Xi'an, China, in 2023. He is currently working toward the Ph.D. degree with the School of Geodesy and Geomatics, Wuhan University, Wuhan, China.

His research interests include deep learning, landslide susceptibility mapping, semantic segmentation for remote sensing, and knowledge graph.

Zhenhong Li (Senior Member, IEEE) received the B.Eng. degree in geodesy from the Wuhan Technical University of Surveying and Mapping (currently Wuhan University), Wuhan, China, in 1997, and the Ph.D. degree in GPS, geodesy, and navigation from the University College London, London, U.K., in 2005.

He is currently a Professor of imaging geodesy with the College of Geological Engineering and Geomatics, Chang'an University, Xi'an, China, the Vice Director with the Key Laboratory of Loess, Xi'an,China, and the Director with the Key Laboratory of Western China's Mineral Resource and Geological Engineering, Ministry of Education, Xi'an, China. He is also a Visiting Professor with the School of Engineering, Newcastle University, Newcastle upon Tyne, U.K. He is also a Principal Investigator with the Generic Atmospheric Correction Online Service (GACOS) for interferometric synthetic aperture radar. He is also the Principal Investigator of the Generic Atmospheric Correction Online Service (GACOS) for interferometric synthetic aperture radar. His research interests include imaging geodesy and its applications to geohazards (e.g., earthquakes, landslides, and land subsidence) and precision agriculture.

Dr. Li is a fellow of the International Association of Geodesy and an Associate Editor of Advances in Space Research and Remote Sensing.

Zhengyang Zhang received the B.S. degree in geographic information science from the Chang'an University, Xi'an, China, in 2024.

His research interest includes deep learning and the application research of Google Earth Engine.

Jing Wu received the B.S. degree in hydrology and water resources engineering from the Hohai University, Nanjing, China, in 2013.

She is currently working with Qinghai Institute of Geo-Environment Monitoring, Xining, China. Her research interests include hydrogeology and groundwater monitoring.

Jianbing Peng received the B.Sc. degree in geology from the China University of Geosciences, Wuhan, China, in 1978, and the Ph.D. degree in engineering geology from the Chang'an University, Xi'an, China, in 1999.

He is currently a Professor of engineering geology with the College of Geological Engineering and Geomatics, Chang'an University. He has more than 40 years of research experience in engineering geology and geohazards (e.g., landslides, ground fissures, and land subsidence).

Dr. Peng is an academician of the Chinese of Academy of Sciences and the President of the Engineering Geology Committee of China.